Single-cell transcriptome analysis reveals cell-cell communication and thyrocyte diversity in the zebrafish thyroid gland.

Pierre Gillotay[1], Meghna Shankar[1], Sema Elif Eski[1], Susanne Reinhardt[2], Annekathrin Kränkel[2], Juliane Bläsche[2], Andreas Petzold[2], Gokul Kesavan[3], Christian Lange[3], Michael Brand[3], Vincent Detours[1], Sabine Costagliola[1]*, Sumeet Pal Singh[1]*

[1] IRIBHM, Université Libre de Bruxelles (ULB), Route de Lennik 808, 1070 Brussels, Belgium.
[2] DRESDEN-concept Genome Center, DFG NGS Competence Center, c/o Center for Molecular and Cellular Bioengineering, TU Dresden, Dresden, 01307, Germany
[3] Center for Molecular and Cellular Bioengineering, TU Dresden, Dresden, 01307, Germany.
* Corresponding authors: scostag@ulb.ac.be; sumeet.pal.singh@ulb.ac.be

Abstract

The thyroid gland regulates growth and metabolism via production of thyroid hormone in follicles composed of thyrocytes. So far, thyrocytes have been assumed to be a homogenous population. To uncover genetic heterogeneity in the thyrocyte population, and molecularly characterize the non-thyrocyte cells surrounding the follicle, we developed a single-cell transcriptome atlas of the zebrafish thyroid gland. The 6249-cell atlas includes profiles of thyrocytes, blood vessels, lymphatic vessels, immune cells and fibroblasts. Further, the thyrocytes could be split into two sub-populations with unique transcriptional signature, including differential expression of the transcription factor *pax2a*. To validate thyrocyte heterogeneity, we generated a CRISPR/Cas9-based *pax2a* knock-in line, which demonstrated specific *pax2a* expression in the thyrocytes. However, a population of *pax2a*-low mature thyrocytes interspersed within individual follicles could be distinguished, corroborating heterogeneity within the thyrocyte population. Our results identify and validate transcriptional differences within the nominally homogenous thyrocyte population.

29 **Keywords**

30 Single-cell, transcriptomics, zebrafish, heterogeneity, thyroid gland, thyroid follicular

31 cells, connective septa, CRISPR/Cas9, knock-in

32 **One-line summary**

33 Single-cell analysis uncovers latent heterogeneity in thyroid follicular cells.

34 **Graphical Abstract**

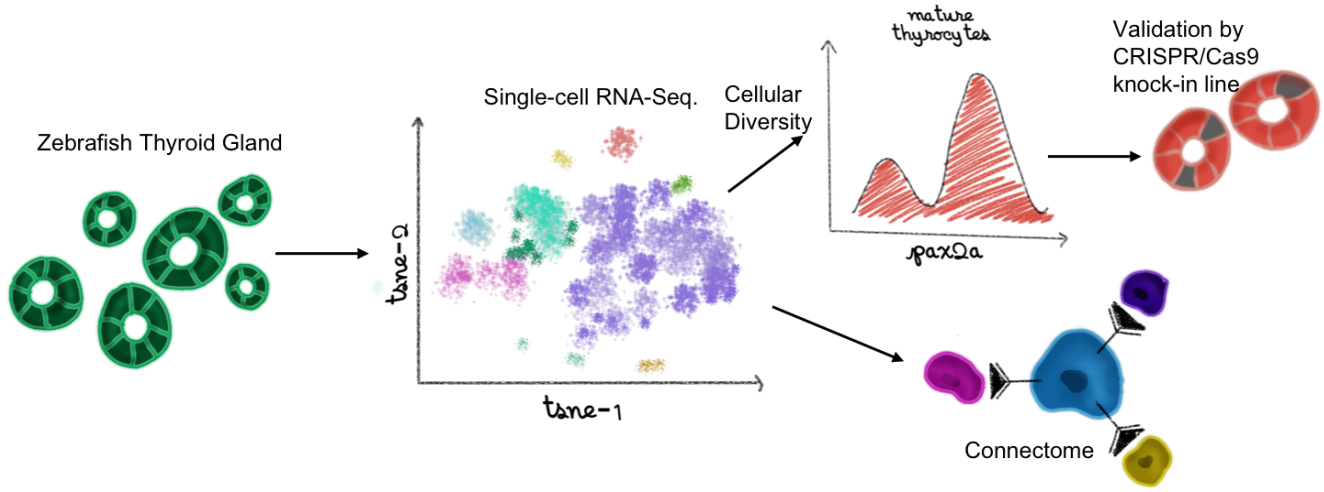

35

Introduction

The thyroid gland produces hormones thyroxine (T4) and triiodothyronine (T3) that regulate body metabolism, growth, and development. Thyroid dysfunction, a disease afflicting almost 100 million people worldwide (1), is common and treatable by hormone replacement. If left untreated, however, it may result in profound adverse effects on the human body, including mental retardation, goiter or dwarfism.

The thyroid gland is an endocrine organ with an intricate structure enabling production, storage and release of the thyroid hormones. It contains numerous variable-sized spherical follicles composed of thyroid follicular epithelial cells, or thyrocytes. The thyrocytes generate the thyroid hormones in a multi-step process. They secrete and store thyroglobulin (TG) in the lumen of the follicles. Additionally, they intake iodide from the blood via sodium-iodide symporter (NIS / Slc5a5). At the interface between thyrocytes and the lumen, thyroid peroxidase (TPO) expressed by the cells catalyzes the coupling of iodide to tyrosyl residues of thyroglobulin (TG). Iodinated TG is absorbed back into the thyrocyte and cleaved by cysteine proteases in lysosomes to form T4 and T3 (2). Though the machinery responsible for the production of thyroid hormones by thyrocytes is well established, it remains unknown if all the thyrocytes resident in the thyroid gland are equally capable of generating thyroid hormones. In other words, the extent of molecular homogeneity between individual thyrocytes has not yet been investigated.

Additionally, the thyroid gland contains many cell-types with potential roles in modulating thyrocyte functionality. The gland contains an extensive distribution of blood vessels, which carry iodide to the thyrocytes and carry thyroid hormones away from

59 them. The thyroid follicles are separated by a mesenchymal cell population, called
60 connective tissue septa, which also divides the gland into lobules. The mammalian
61 thyroid gland also contains parafollicular epithelial cells, or C-cells, that synthesize and
62 secrete the hormone calcitonin. These parafollicular epithelial cells are, however,
63 located outside the thyroid gland in fish and amphibians (3). Further, the presence of
64 immune cells and innervation has been demonstrated within the thyroid gland (4, 5).
65 Though we have a considerable understanding of these cell-types on a histological
66 level, we still lack the molecular characterization of the thyroid gland cell ensemble. This
67 extends to an incomplete appreciation of the impact of the diverse cell-populations on
68 thyroid follicular cell physiology.
69 To uncover the diversity within the thyrocyte population, and further characterize
70 the surrounding tissue at cellular resolution, we develop the first atlas of the thyroid
71 gland at single-cell resolution. For this, we build on the progress in single-cell
72 transcriptomics (6) to transcriptionally profile thousands of individual cells isolated from
73 the thyroid gland of adolescent and adult zebrafish. We demonstrate that these profiles
74 comprehensively represent the cells present in the zebrafish thyroid gland. Further, we
75 demonstrate the segregation of thyrocytes into two transcriptionally distinct sub-
76 populations. Utilizing the expression profiles of discrete cell populations, we build an
77 intercellular signaling network to uncover communication between thyrocytes and the
78 surrounding tissue. Finally, to enable easy access to the data, we have made the
79 zebrafish thyroid gland atlas available for online browsing.

Results

Single-cell transcriptomics of the zebrafish thyroid gland.

To generate the molecular catalogue of the thyroid gland at cellular resolution, we sampled the organ from two ages of zebrafish: 2 month post-fertilization (mpf) and 8 mpf (Supp. Figure 1). The time points span adolescent to adult transition in zebrafish, with animals containing fully differentiated functional organs at both stages. By 2 mpf, the adolescent animals have completed morphogenesis, but are yet to reach sexual maturity. The animals sampled at 2 mpf were on average 2.6 cm in length and 123.8 mg in weight. In contrast, fish at 8 mpf are sexually mature adults, with an average length of 3.5 cm and an average weight of 294.4 mg (Supp. Figure 1). To characterize the organ cell-types in an unbiased manner, we dissected out the entire thyroid gland (Fig. 1A, B) from six animals at each stage, and prepared the single-cell suspension for cDNA library preparation. To guide thyroid gland dissection, we utilized the *Tg(tg:nls-mVenus-T2A-NTR)* zebrafish reporter line (7) that labels thyrocytes with bright yellow fluorescent protein (Fig. 1B'). The micro-dissected tissue was dissociated using enzymatic digestion. The single-cell suspension was stained with calcein, which specifically labels live cells with blue fluorescence. The live cells were then enriched using FACS (Supp. Figure 2) to limit false positive signals from dead and/or ruptured cells (8). Twelve thousand live-cells, pooled from six animals, were collected in separate tubes according to age and profiled using droplet-based high-throughput single-cell RNA-sequencing provided by 10X Genomics (9, 10). The 10X Genomics pipeline uses molecule and cell-specific barcoding allowing transcript quantification without amplification bias (11, 12). Using the Cell Ranger bioinformatics pipelines, the resulting Next-Generation

Sequencing libraries were mapped to the zebrafish genome, de-multiplexed according to their cellular barcodes and quantified to generate gene/cell UMI (unique molecular identifier) count tables. Quality-based exclusion of single-cell transcriptomes was implemented based on mean library size, percentage of mitochondrial reads and number of genes detected per cell. On average, we detected 6012 UMIs and 1303 genes per cell (Supp. Figure 3). The process recovered in total 6249 cells, providing single-cell transcriptomic profiles for 2986 and 3263 individual cells for 2 mpf and 8 mpf, respectively.

Identification of cell-types present in the zebrafish thyroid gland.

To aid with visualization of the zebrafish thyroid gland single-cell RNA-Seq (scRNA-Seq) data, we projected the cellular profiles onto t-distributed stochastic neighbor embedding (t-SNE) plots, a non-linear dimensionality reduction technique (13) (Fig. 1C). Using unsupervised graph-based clustering, we identified seven clusters for the thyroid gland. Using the expression of genes involved in thyroid hormone production, we could identify one of the clusters as thyroid follicular cells (Fig. 1D – F). The cluster, labeled as thyrocytes, contains 267 cells.

To define the identity of the remaining cell clusters, we generated cluster-specific marker genes by performing differential gene expression analysis (Fig. 2A) (Supp. Table 1). For four clusters, the marker genes included one or more known cell type–specific identifiers. This included *gpr182* for endothelial cells; *acta2* for musculature; *fcer1gl* for immune cells; and *ponzr3* for cells from zebrafish gills (Fig. 2B – E). Based on these cell identifiers, the atlas includes 233 endothelial cells, 135 muscle lineage cells, 914 immune cells and 199 cells from zebrafish gills. Notably, the endothelial cell

126 cluster includes blood vessels (*flt1* and *kdrl*) and lymphatic vessels (*mrc1a*, *prox1a*, *flt4*
127 and *lyve1b*) (Supp. Fig. 4); while the immune cell cluster includes macrophages
128 (*mpeg1.1* and *mfap4*), neutrophils (*lyz*) and lymphocytes (*il4*, *il13* and *il11b*) (Supp. Fig.
129 5).

130 For the remaining two clusters (number six and seven), we identified marker
131 genes that hinted towards identity of the cell-type. Specifically, *col1a2* and *tp63*
132 enriched in cluster number six and seven respectively (Fig. 2 F – G), are known
133 markers of fibroblasts (14, 15) and epithelial tissue (16–18). We performed gene-
134 ontology (GO) enrichment analysis of the marker genes to aid with classification (Supp.
135 Fig. 6). Cluster six demonstrated an enrichment of 'extracellular matrix structural
136 constituent', 'connective tissue development' and 'extracellular space', confirming the
137 presence of tissue fibroblasts in this cluster. Thus, we labelled cluster six as 'Stromal'
138 cells. Cluster seven displayed an enrichment of 'cell motility', 'cell migration' and
139 'epithelium development', suggestive of epithelial cells. Hence, we labelled cluster
140 seven as 'Non-Follicular Epithelium (NFE)', to distinguish them from the thyroid follicular
141 epithelial cells. Our data contains 3670 stromal cells and 831 non-follicular epithelial
142 cells.

143 Our marker gene identification further established additional genes enriched in a
144 single cell-type in the thyroid gland (Fig. 2A) (Supp. Table 1). For instance, we identified
145 *cx30.3*, a connexin gene and *prdx1*, a gene involved in the antioxidant response, to be
146 specifically expressed in the thyrocytes. To enable further investigation of the clusters
147 and gene expression profiles, we have developed an interactive webtool for online
148 browsing (https://sumeet.shinyapps.io/zfthyroid/).

Development of autocrine and paracrine signaling networks in the thyroid gland using known ligand-receptor interactions.

Having defined the cell types of the thyroid gland, we quantified potential cell-cell interactions between thyrocytes and all cell types present in the organ (Fig. 3A) based on a reference list of approximately 3,100 literature-supported interactions containing receptors and ligands from receptor tyrosine kinase (RTK), extracellular matrix (ECM)-integrin, chemokine and cytokine families (19). Although anatomical barriers between cell types are not modeled in this analysis, expression patterns of ligand-receptor pairs revealed a dense intercellular communication network (Fig. 3B). The network consisted of 322 ligands expressed on different cell-types with a corresponding receptor expressed on the thyrocytes (Supp. Table 2). For instance, the stromal cells express the ligand *lpl* (Lipoprotein Lipase) that signals through the *lrp2a* (zebrafish homologue of Megalin) receptor (Fig. 3C). Stromal and muscle cells express *dcn* (Decorin) whose receptor *met* is expressed by thyrocytes. Further, the ligand *cyr61* is broadly expressed in the thyroid gland, with one of its receptors, *itgb5*, an integrin isoform, expressed specifically by the thyrocytes. The identified interactions also include autocrine signaling. For example, the ligand *sema3b* and its receptor *nrp2a* are both present on thyrocytes. GO-analysis for identified ligand-receptor pairs revealed genes involved in 'PI3K-Akt signaling pathway', 'MET signaling' and 'integrin binding' (Supp. Fig. 7).

Thyrocytes are composed of transcriptionally distinct sub-populations.

Next, we characterized the transcriptional differences within the thyrocyte population. For this, we bioinformatically isolated the thyrocytes, and re-performed the

clustering pipeline on the isolated cell population. With this, we could segregate the thyrocytes into two smaller clusters (Fig. 4A), labeled as 'Cluster_Blue' and 'Cluster_Red'. The two clusters displayed differences in the expression levels of 265 genes (Fig. 4B) (Supp. Table 3). Notably, Cathepsin B (*ctsba*) is significantly downregulated in the blue cluster (Fold change = 1.6, p-value = $1.47x10^{-9}$) (Fig. 4B – C). Cathepsin B is a cysteine protease that is involved in the processing of iodinated thyroglobulin to T4 and T3 in the thyrocyte lysosomes (2, 20). Moreover, fusion of Cathepsin B and EGFP has been previously used to track thyroid hormone processing lysosomes in rat thyroid epithelial cell lines (21).

Along with higher expression of Cathepsin B, the red cluster displayed significant downregulation of *pax2a* expression (Fold change = 1.7, p-value = $8.24x10^{-9}$) (Fig. 4B-C). *pax2a* belongs to the PAX (paired box DNA-binding) domain containing family of transcription factors. The loss of *pax2a* expression in the red cluster is notable, as *pax2a* is an important regulator of thyrocyte development (22). Zebrafish thyroid primordium expresses *pax2a* at 24 hpf (22), which is required for specification of the thyroid follicles (23, 24). Consequently, zebrafish lacking *pax2a* fail to develop thyroid follicles (22), which is similar to the Pax8 knock-out phenotype in mouse (25). The low expression of *pax2a* in the red cluster, without a difference in *tg* expression, suggests the presence of a thyrocyte sub-population with a distinct gene expression signature.

Generation of *pax2a* knock-in reporter line.

To validate the heterogeneity among the zebrafish thyrocytes, we focused on the expression of *pax2a* transcription factor. We generated a knock-in line by inserting monomeric Kusabira Orange 2 (mKO2) fluorescent protein to the 3' end of the

194 endogenous *pax2a* genomic location (Fig. 5A). The *pax2a*$^{pax2a\text{-}T2A\text{-}mKO2}$ (abbreviated as
195 *pax2a*^{mKO2}) reporter expression perfectly overlapped with PAX2A antibody staining at 9.5
196 hours post-fertilization (Fig. 5B). Moreover, the knock-in line displayed mKO2
197 fluorescence in the otic vesicle, mid-hindbrain boundary, optic stalk, pronephros and the
198 thyroid gland (Fig. 5C – F, Supp. Movie 1), mimicking known expression of *pax2a* during
199 zebrafish development (26). Additionally, in order to assess whether the dynamics of
200 mKO2 expression would follow modifications in the expression of endogenous *pax2a,* we
201 used CRISPR/Cas9 technology to generate F0 knock-outs (also known as Crispant (27))
202 of *pax2a* gene in our *pax2a*^{mKO2} line. The crispants displayed defects in thyroid
203 morphogenesis (Fig. 8G – H), mimicking the phenotype of *pax2a* loss-of-function
204 mutation (22). Live imaging of crispants at 55 hpf revealed strong decrease of mKO2
205 expression (Fig. 8G – H), thereby corroborating the faithful recapitulation of *pax2a*
206 expression by the newly generated reporter line.

207 **Segregation of thyrocyte sub-populations based on *pax2a* reporter expression.**

208 Upon investigating the fluorescence expression of the *pax2a* reporter in the
209 thyroid gland of adult zebrafish, we found strong and specific expression of *pax2a*
210 reporter in the thyrocytes lining the thyroid follicles (Fig. 6A – D). Although a majority of
211 thyrocytes displayed uniform expression of *pax2a* reporter, we could identify a small
212 population of *pax2a*^{mKO2}-Low thyrocytes (Fig. 6B – D). The *pax2a*^{mKO2}-Low thyrocytes
213 were not segregated, but scattered throughout the gland, thereby suggesting a mixing
214 of the two thyrocyte sub-populations.

215 To quantify the proportions of *pax2a*^{mKO2}-Low and -High thyrocytes, we
216 performed FACS analysis on *pax2a*^{mKO2}; *Tg(tg:nls-EGFP)* double transgenic line (Fig.

6E – G). The *Tg(tg:nls-EGFP)* zebrafish line labels the thyrocyte population in green fluorescence (27). We restricted our analysis to the thyrocyte population by gating for GFP+ cells in the thyroid gland (Fig. 6E). Within the thyrocyte population, the cells displayed a normal distribution of GFP fluorescence; however, thyrocytes could be split into two sub-populations based on the levels of *pax2a* reporter expression (Fig. 6F – G). Specifically, 75% of thyrocytes (202 out of 268 cells) displayed *pax2a*^{mKO2}-High fluorescence, while 25% of thyrocytes (66 out of 268 cells) displayed *pax2a*^{mKO2}-Low fluorescence levels.

In summary, the analysis of *pax2a* knock-in line validates the identification of thyrocyte sub-populations within our single-cell RNA-Seq. data, and clearly demonstrates, for the first time, the presence of transcriptionally diverse sub-populations of thyrocytes present in the thyroid gland.

Discussion

We have applied for the first time unbiased single-cell gene expression analysis to the thyroid gland. In contrast with the mainstream view that thyrocytes constitute a molecularly uniform population, we identify two transcriptionally distinct sub-populations of thyrocytes. The two sub-populations differed, among other genes (Supp. Table 3), in the expression levels of a transcription factor *pax2a* and a cysteine protease Cathepsin B (*ctsba*) (Fig. 4B – C). Cathepsin B is particularly notable as it enables the liberation of thyroid hormone from thyrocytes by proteolytic processing of thyroglobulin (2, 20).

We validate the heterogeneity among the thyrocytes using a newly generated knock-in reporter line for *pax2a* gene (Fig. 5). The knock-in reporter line was generated using CRISPR/Cas9-based insertion of mKO2 fluorescent protein in the endogenous *pax2a* genomic location. The *pax2a* knock-in line faithfully recapitulates the embryonic expression of *pax2a* gene (Supp. Movie 1, Fig. 5B – F). Using the *pax2a* reporter line to characterize the adult thyroid gland, we demonstrate the presence of *pax2a*^{mKO2}-Low thyrocytes in the follicles (Fig. 6). Notably, *pax2a*^{mKO2}-Low and *pax2a*^{mKO2}-High thyrocytes are present in the same follicle (Fig. 6C – D), raising the possibility of contact-mediated interactions between the two sub-populations. It would be of interest to build on this study and investigate the functional and replicative differences among the two sub-populations of thyrocytes.

Our single-cell transcriptomics atlas provides a comprehensive genomics resource to study the zebrafish thyroid gland in unprecedented detail. We performed unbiased profiling of the thyroid gland, without enrichment for a specific cell-type. This allowed us to capture yet poorly characterized cell-populations within the thyroid gland.

Specifically, we provide the molecular characteristics of the stromal tissue present in the zebrafish thyroid gland. The stromal cells display enrichment of extra-cellular matrix (ECM) related genes (Supp. Table 1) and are possibly homologous to the mesenchymal connective septa found in the mammalian thyroid gland. The connective septa helps cluster the thyroid follicles into lobules. Notably, the expression of fgf ligands from the mesenchymal septa cells has been implicated in lobe formation during mouse thyroid gland development (28). It would be of interest to test if similar morphological clustering of the thyroid follicles exists in zebrafish, and the role the stromal cells play during development and growth of the thyrocytes.

Our atlas further identifies a non-follicular epithelial (NFE) cell-population present in the zebrafish thyroid gland. It is interesting to note that epithelial cells apart from follicular and parafollicular cells have been observed in the mammalian thyroid gland. In a report from E. Baber published in 1876 (29), histological examination of the dog thyroid gland displayed the presence of cells “beside the stroma, lymphatics, blood vessels, & cells between the vesicles”. Dr. Baber labeled the cells as ‘parenchyma’, and noted the existence of “numerous cells differing markedly in size and shape from the epithelial cells amongst which they lie” (29). Recently, epithelial cells have been reported in a structure called the Solid Cell Nests (SCN) of the thyroid (30). SCN are lumen containing irregular structures located between the thyroid lobes in mammals. SCN contain two types of epithelial cells: main cells and C-cells, expressing TP63 and calcitonin respectively (31). Notably, the NFE cells we identified in the zebrafish thyroid gland are marked with TP63 expression (Fig. 2G), raising the possibility of their homology with the main cells of the SCN. C-cells, however, exist outside the thyroid

gland in zebrafish (3), and thus it is unlikely that the NFE cells we have identified would be related to cells of parafollicular origin. Currently, the developmental origin of NFE cells and their role in thyroid gland is unclear. To study the cell-population, transgenic zebrafish reagents driving expression using the *tp63* regulatory region (32) could be utilized in future.

To survey the communication between thyrocytes, the functional unit of the thyroid gland, and the other cell-types present in the thyroid gland, we constructed a cellular interaction network (Fig. 3B). The network was built by matching the expression of ligands in the diverse cell-types with the expression of receptor in the thyrocytes (Supp. Table 2) (19). Based on literature survey, we manually identified multiple interacting genes that have been implicated in thyroid diseases. For instance, the ligand Decorin (*dcn*) is expressed by the stromal cells and musculature, with its receptor, MET, present on thyrocytes (Fig. 3C). Decorin, a secreted proteoglycan, is considered a "guardian from the matrix" (33), as it is an antagonist of growth factor signaling. Importantly, Decorin expression has been reported to be downregulated in thyroid cancer samples (34). Thus, stromal cells could modulate Decorin to control thyrocytes growth. Further, interactions for CYR61 (associated with Graves' Disease (35)), LRP2 / Megalin (involved in thyroglobulin processing (36)) and NRP2 (associated thyroid cancer metastasis (37)) were identified (Fig. 3C). The hypothesis generated by the theoretical ligand-receptor interaction network can be tested *in vivo* in zebrafish or *in vitro* by manipulation of thyrocytes in thyroid organoid models (38) to gain valuable insight into thyroid gland homeostasis.

297 The current atlas is restricted to healthy adolescent and adult thyroid gland. In
298 future, it would be of interest to extend the atlas by including single-cell transcriptomics
299 from embryonic and old fish, providing a comprehensive resource for development,
300 homeostasis and aging of the thyroid gland. It would be of further interest to profile
301 zebrafish models of thyroid disorder (39, 40) to understand the cellular and molecular
302 changes underlying organ dysfunction. Combined with the power of CRISPR/Cas9
303 based screen that we have established for the thyroid gland (27), this resource will
304 provide a roadmap for the functional elucidation of cell type specific programs during
305 thyroid gland growth and homeostasis.
306 In summary, our work provides the first molecular map of the zebrafish thyroid
307 gland at cellular resolution. The atlas contains the molecular characterization of the
308 thyroid gland stromal population, identification of non-follicular epithelial cells, and
309 demonstrate the transcriptional heterogeneity among zebrafish thyrocytes. Further, by
310 constructing cell-cell communication network, the atlas provides clues into tissue
311 dynamics present within the organ. Finally, the dataset has been made available for
312 browsing via an interactive webtool (https://sumeet.shinyapps.io/zfthyroid/). We hope
313 that our efforts will expand the understanding of thyrocytes beyond a nominally
314 homogenous endocrine cell population; providing a complex picture of the diversity in
315 thyrocyte identity and function.
316

Methods

Zebrafish strains and husbandry

Wild-type or transgenic zebrafish of the outbred AB, WIK, or a hybrid WIK/AB strain were used in all experiments. Zebrafish were raised under standard conditions at 28 °C. Animals were chosen at random for all experiments. Published transgenic strains used in this study were *Tg(tg:nls-mVenus-T2A-NTR)* (7) and *Tg(tg:nls-GFP)* (27). Experiments with *Tg(tg:nls-mVenus-T2A-NTR)* were conducted in accordance with the Animal Welfare Act and with permission of the Landesdirektion Sachsen, Germany (DD24-5131/346/11, DD24-5131/346/12, DD24.1-5131/476/2, TVV21/2018 and all corresponding amendments). Zebrafish husbandry and experiments with *Tg(tg:nls-GFP)* and *pax2a* knock-in line were performed under standard conditions in accordance with institutional (Université Libre de Bruxelles (ULB)) and national ethical and animal welfare guidelines and regulation, which were approved by the ethical committee for animal welfare (CEBEA) from the Université Libre de Bruxelles (protocols 578N-579N).

Single cell suspension of zebrafish thyroid gland

Single cell suspension of zebrafish thyroid gland was performed by adapting the cell dissociation protocol outlined in Singh et al., Scientific Reports, 2018 (41). In brief, the thyroid gland was collected and dissociated into single cells by incubation in TrypLE (ThermoFisher, 12563029) with 0.1% Pluronic F-68 (ThermoFisher, 24040032) at 37 °C in a benchtop shaker set at 450 rpm for 45 min. Following dissociation, TrypLE was inactivated with 10% FBS, and the cells pelleted by centrifugation at 500g for 10min at 4 °C. The supernatant was carefully discarded and the pellet re-suspended in 500 uL of

HBSS (without Ca, Mg) + 0.1% Pluronic F-68. To remove debris, the solution was passed over a 30 µm cell filter (Miltenyi Biotec, 130-041-407). To remove dead cells, calcein violet (ThermoFisher, C34858) was added at a final concentration of 1 µM and the cell suspension incubated at room temperature for 20 minutes. The single cell preparation was sorted with the appropriate gates, including excitation with UV (405 nm) laser for identification of alive cells (calcein+). FACS was performed through 100 µm nozzle.

Single-cell profiling of the zebrafish thyoid gland

For single-cell RNA-seq of the zebrafish thyroid gland using the 10X Genomics platform, cell suspension was prepared as mentioned above from the thyroid glands of six 2 month post fertilization and six 8 month post-fertilization *Tg(tg:nls-mVenus-T2A-NTR)* animals. The cell suspension was adjusted with Hanks' Balanced Salt Solution (without calcium and magnesium) to a density of 800cells/µl, and diluted with nuclease-free water according to the manufacturer's instructions to yield 12,000 cells. Subsequently, the cells were carefully mixed with reverse transcription mix before loading the cells on the 10X Genomics Chromium system (10). After the gel emulsion bead suspension underwent the reverse transcription reaction, emulsion was broken and DNA purified using Silane beads. The complementary DNA was amplified with 10 cycles, following the guidelines of the 10x Genomics user manual. The 10X Genomics single cell RNA-seq library preparation—involving fragmentation, dA tailing, adapter ligation and indexing PCR—was performed based on the manufacturer's protocol. After quantification, the libraries were sequenced on an Illumina NextSeq 550 machine using a HighOutput flowcell in paired-end mode (R1: 26 cycles; I1: 8 cycles; R2: 57 cycles),

thus generating ~45mio fragments. The raw sequencing data were then processed with the 'count' command of the Cell Ranger software (v.2.1.0) provided by 10x Genomics with the option '–expect-cells' set to 10,000 (all other options were used as per default). To build the reference for Cell Ranger, zebrafish genome (GRCz10) as well as gene annotation (Ensembl 87) were downloaded from Ensembl and the annotation was filtered with the 'mkgtf ' command of Cell Ranger (options: '–attribute=gene_biotype:protein_coding– attribute=gene_biotype:lincRNA –attribute=gene_biotype:antisense'). Genome sequence and filtered annotation were then used as input to the 'mkref ' command of Cell Ranger to build the appropriate Cell Ranger Reference.

Analysis of single-cell RNA-Seq. of the zebrafish thyroid gland

The raw data generated from 10x Chromium pipeline was clustered using Seurat 2.3.4 (42) using the recommended analysis pipeline. Briefly, the raw data as UMI-counts was log-normalized, regressed to remove the effect of library size and mitochondrial counts, and scaled. Highly variable genes were identified for PCA analysis and graph-based clustering. Marker genes identified for each cluster were used to classify the cell-type. The thyrocyte cluster was isolated and sub-clustered to identify and label sub-populations.

Data Availability

The raw 10X data, along with tabulated count data are available publicly from GEO under accession number GSE133466. The atlas for online browsing is available at https://sumeet.shinyapps.io/zfthyroid/.

Generation of knock-in *pax2a*$^{pax2a\text{-}T2A\text{-}mKO2}$ zebrafish line

For generation of *pax2a* reporter line, we designed a single-guide RNA (sgRNA) targeting the STOP codon of the *pax2a* coding sequence (GCTGCGATGGTAACTAGTGG). We then generated a donor construct in which the sequence encoding for the monomeric Kusabira orange (mKO2) protein was fused to a viral 2A peptide linker. This reporter cassette was flanked by left (1000bp) and right (2000bp) homology arms of the *pax2a* genomic DNA region around the stop codon therefore preventing the sgRNA from cutting the donor construct. sgRNA design, production and validation were done as previously described (27, 43). Wild-type embryos were injected with 3 nL of the injection mix containing the sgRNA (final concentration 80 ng/µL), the donor construct (final concentration 7.5 ng/µL), the protein Cas9 (recombinant cas protein from *S. pyogenes* PNA Bio CP01, final concentration 100 ng/µL) and KCL (final concentration 200 mM). Upon homologous recombination of this reporter construct in the endogenous locus, *pax2a*-expressing cells were fluorescently labelled by mKO2. This *pax2a*$^{pax2a\text{-}T2A\text{-}mKO2}$ line is referenced as *pax2a*^{mKO2} in the text.

Generation of *pax2a* crispants

Somatic mutagenesis of pax2a gene was carried out exactly as mentioned in Trubiroha et al., Scientific Reports, 2018 (27). Briefly, sgRNA targeting the exon 2 of *pax2a* was generated as described in the publication. Following the strategy described in the publication, Cas9 protein along with sgRNA was injected in one-cell stage of zebrafish embryos for disruption of *pax2a* gene. Non-injected animals were used as controls.

Tissue collection

To facilitate confocal imaging of the thyroid gland, the organ was dissected from fish after fixation. Fish were killed in Tricaine prior to either direct fixation or dissection of the gland, and the samples immersed in 4% paraformaldehyde + 1% Triton-X overnight at 4 °C. The gland was then manually dissected and washed multiple times in PBS.

Immunofluorescence and image acquisition

Whole-mount immunofluorescence was performed on thyroid gland collected as described above. The collected samples were permeabilized in 1% PBT (Triton-X-100) and blocked in 4% PBTB (BSA). Primary and secondary antibody stainings were performed overnight at 4 °C. Primary antibodies used in this study were anti-PAX2A (rabbit, Genetex GTX128127) at 1:250, anti-EGFP (chicken, Abcam ab13970) at 1:1000, anti-E-Cadherin (mouse, BD bioscience cat 610181) at 1:200, anti-monomeric Kusabira-Orange 2 (mouse, MBL amalgaam M-168-3M) at 1:200 and anti-monomeric Kusabira-Orange 2 (rabbit, MBL amalgam PM051M) at 1:250. Secondary antibodies at 1:250 dilutions used in this study were Alexa Fluor 488 anti-chicken (Jackson ImmunoResearch laboratories 703-545-155), Alexa Fluor 647 anti-rabbit (Jackson ImmunoResearch laboratories 711-605-152), Alexa Fluor 647 anti-mouse (Jackson ImmunoResearch laboratories 715-605-150), Cy™3-conjugated anti-rabbit (Jackson ImmunoResearch laboratories 711-165-152) and Cy™3-conjugated anti-mouse (Jackson ImmunoResearch laboratories 715-165-150). When needed nuclei were staining using DAPI at a 1:1000 dilution. Samples were mounted in NuSieve™ GTG™ Agarose (Lonza cat50080) and imaged on a glass bottom FluoroDish™ (WPI FD3510-100) using a Zeiss LSM 780

confocal microscope or Leica DMI 6000b microscope. ImageJ was used to add scale bars and PowerPoint was used for adding arrows and labels.

FACS-based reporter analysis

For analysing the levels of *pax2a*^{mKO2} by FACS, single-cell suspension from the thyroid gland of 5 mpf *Tg(tg:nls-GFP)*; *pax2a*^{mKO2} animals was prepared as described earlier and stained with 1 µM calcein violet (ThermoFisher, C34858). Cells were sorted and analyzed using FACS-Aria II (BD Bioscience). Thyrocytes were selected by gating for calcein+ GFP+ population, and mKO2 expression level recorded for analysis.

Gene Ontology (GO) Analysis

Gene ontology (GO) analysis was performed using DAVID (44). The list of genes was uploaded on the web browser of DAVID and statistically significant (p-value < 0.05) GO terms were identified using default parameters.

Statistical analysis

Statistical analysis was performed using R. No animals were excluded from analysis. Blinding was not performed during analysis. Analysis of normal distribution was not performed.

References

1. Taylor PN, Albrecht D, Scholz A, Gutierrez-Buey G, Lazarus JH, Dayan CM, Okosieme OE 2018 Global epidemiology of hyperthyroidism and hypothyroidism. Nat Rev Endocrinol **14**:301–316.
2. Brix K, Lemansky P, Herzog V 1996 Evidence for extracellularly acting cathepsins mediating thyroid hormone liberation in thyroid epithelial cells. Endocrinology **137**:1963–74.
3. Alt B, Reibe S, Feitosa NM, Elsalini OA, Wendl T, Rohr KB 2006 Analysis of origin and growth of the thyroid gland in zebrafish. Dev Dyn **235**:1872–1883.
4. Linehan SA, Martínez-Pomares L, da Silva RP, Gordon S 2001 Endogenous ligands of carbohydrate recognition domains of the mannose receptor in murine macrophages, endothelial cells and secretory cells; potential relevance to inflammation and immunity. Eur J Immunol **31**:1857–66.
5. Nonidez JF 1931 Innervation of the thyroid gland. II. Origin and course of the thyroid nerves in the dog. Am J Anat **48**:299–329.
6. Svensson V, Vento-Tormo R, Teichmann SA 2018 Exponential scaling of single-cell RNA-seq in the past decade. Nat Protoc **13**:599–604.
7. McMenamin SK, Bain EJ, McCann AE, Patterson LB, Eom DS, Waller ZP, Hamill JC, Kuhlman JA, Eisen JS, Parichy DM 2014 Thyroid hormone-dependent adult pigment cell lineage and pattern in zebrafish. Science (80-) **345**:1358–1361.
8. AlJanahi AA, Danielsen M, Dunbar CE 2018 An Introduction to the Analysis of Single-Cell RNA-Sequencing Data. Mol Ther Methods Clin Dev **10**:189–196.
9. Macosko EZ, Basu A, Satija R, Nemesh J, Shekhar K, Goldman M, Tirosh I,

Bialas AR, Kamitaki N, Martersteck EM, Trombetta JJ, Weitz DA, Sanes JR, Shalek AK, Regev A, McCarroll SA 2015 Highly Parallel Genome-wide Expression Profiling of Individual Cells Using Nanoliter Droplets. Cell **161**:1202–1214.

10. Zheng GXY, Terry JM, Belgrader P, Ryvkin P, Bent ZW, Wilson R, Ziraldo SB, Wheeler TD, McDermott GP, Zhu J, Gregory MT, Shuga J, Montesclaros L, Underwood JG, Masquelier DA, Nishimura SY, Schnall-Levin M, Wyatt PW, Hindson CM, Bharadwaj R, Wong A, Ness KD, Beppu LW, Deeg HJ, McFarland C, Loeb KR, Valente WJ, Ericson NG, Stevens EA, Radich JP, Mikkelsen TS, Hindson BJ, Bielas JH 2017 Massively parallel digital transcriptional profiling of single cells. Nat Commun **8**:14049.

11. Kivioja T, Vähärautio A, Karlsson K, Bonke M, Enge M, Linnarsson S, Taipale J 2011 Counting absolute numbers of molecules using unique molecular identifiers. Nat Methods **9**:72–4.

12. Islam S, Zeisel A, Joost S, La Manno G, Zajac P, Kasper M, Lönnerberg P, Linnarsson S 2014 Quantitative single-cell RNA-seq with unique molecular identifiers. Nat Methods **11**:163–6.

13. Maaten L van der, Hinton G 2008 Visualizing data using t-SNE. J Mach Learn Res **9**:2579–2605.

14. Sánchez-Iranzo H, Galardi-Castilla M, Sanz-Morejón A, González-Rosa JM, Costa R, Ernst A, Sainz de Aja J, Langa X, Mercader N 2018 Transient fibrosis resolves via fibroblast inactivation in the regenerating zebrafish heart. Proc Natl Acad Sci U S A **115**:4188–4193.

15. Denton CP, Zheng B, Shiwen X, Zhang Z, Bou-Gharios G, Eberspaecher H, Black CM, de Crombrugghe B 2001 Activation of a fibroblast-specific enhancer of the proalpha2(I) collagen gene in tight-skin mice. Arthritis Rheum **44**:712–22.

16. Lisse TS, Middleton LJ, Pellegrini AD, Martin PB, Spaulding EL, Lopes O, Brochu EA, Carter E V, Waldron A, Rieger S 2016 Paclitaxel-induced epithelial damage and ectopic MMP-13 expression promotes neurotoxicity in zebrafish. Proc Natl Acad Sci U S A **113**:E2189-98.

17. Reischauer S, Levesque MP, Nüsslein-Volhard C, Sonawane M 2009 Lgl2 executes its function as a tumor suppressor by regulating ErbB signaling in the zebrafish epidermis. PLoS Genet **5**:e1000720.

18. Barbieri CE, Pietenpol JA 2006 p63 and epithelial biology. Exp Cell Res **312**:695–706.

19. Ramilowski JA, Goldberg T, Harshbarger J, Kloppman E, Lizio M, Satagopam VP, Itoh M, Kawaji H, Carninci P, Rost B, Forrest ARR 2015 A draft network of ligand-receptor-mediated multicellular signalling in human. Nat Commun **6**:7866.

20. Brix K, Linke M, Tepel C, Herzog V 2001 Cysteine proteinases mediate extracellular prohormone processing in the thyroid. Biol Chem **382**:717–25.

21. Linke M 2002 Trafficking of lysosomal cathepsin B--green fluorescent protein to the surface of thyroid epithelial cells involves the endosomal/lysosomal compartment. J Cell Sci **115**:4877–4889.

22. Wendl T, Lun K, Mione M, Favor J, Brand M, Wilson SW, Rohr KB 2002 Pax2.1 is required for the development of thyroid follicles in zebrafish. Development **129**:3751–60.

513 23. Porazzi P, Calebiro D, Benato F, Tiso N, Persani L 2009 Thyroid gland
514 development and function in the zebrafish model. Mol Cell Endocrinol **312**:14–23.
515 24. Pfeffer PL, Gerster T, Lun K, Brand M, Busslinger M 1998 Characterization of
516 three novel members of the zebrafish Pax2/5/8 family: dependency of Pax5 and
517 Pax8 expression on the Pax2.1 (noi) function. Development **125**:3063–74.
518 25. Mansouri A, Chowdhury K, Gruss P 1998 Follicular cells of the thyroid gland
519 require Pax8 gene function. Nat Genet **19**:87–90.
520 26. Kesavan G, Chekuru A, Machate A, Brand M 2017 CRISPR/Cas9-Mediated
521 Zebrafish Knock-in as a Novel Strategy to Study Midbrain-Hindbrain Boundary
522 Development. Front Neuroanat **11**:52.
523 27. Trubiroha A, Gillotay P, Giusti N, Gacquer D, Libert F, Lefort A, Haerlingen B, De
524 Deken X, Opitz R, Costagliola S 2018 A Rapid CRISPR/Cas-based Mutagenesis
525 Assay in Zebrafish for Identification of Genes Involved in Thyroid Morphogenesis
526 and Function. Sci Rep **8**:5647.
527 28. Liang S, Johansson E, Barila G, Altschuler DL, Fagman H, Nilsson M 2018 A
528 branching morphogenesis program governs embryonic growth of the thyroid
529 gland. Development **145**:dev146829.
530 29. Baber EC 1876 XXI. Contributions to the minute anatomy of the thyroid gland of
531 the dog. Philos Trans R Soc London **166**:557–568.
532 30. Harach HR 1988 Solid cell nests of the thyroid. J Pathol **155**:191–200.
533 31. Ríos Moreno MJ, Galera-Ruiz H, De Miguel M, López MIC, Illanes M, Galera-
534 Davidson H 2011 Inmunohistochemical profile of solid cell nest of thyroid gland.
535 Endocr Pathol **22**:35–9.

536 32. Rasmussen JP, Sack GS, Martin SM, Sagasti A 2015 Vertebrate epidermal cells
537 are broad-specificity phagocytes that clear sensory axon debris. J Neurosci
538 **35**:559–70.
539 33. Neill T, Schaefer L, Iozzo R V 2012 Decorin: a guardian from the matrix. Am J
540 Pathol **181**:380–7.
541 34. Martínez-Aguilar J, Clifton-Bligh R, Molloy MP 2016 Proteomics of thyroid
542 tumours provides new insights into their molecular composition and changes
543 associated with malignancy. Sci Rep **6**:23660.
544 35. Planck T, Shahida B, Sjögren M, Groop L, Hallengren B, Lantz M 2014
545 Association of BTG2, CYR61, ZFP36, and SCD gene polymorphisms with
546 Graves' disease and ophthalmopathy. Thyroid **24**:1156–61.
547 36. Marinò M, McCluskey RT 2000 Megalin-mediated transcytosis of thyroglobulin by
548 thyroid cells is a calmodulin-dependent process. Thyroid **10**:461–9.
549 37. Tu D-G, Chang W-W, Jan M-S, Tu C-W, Lu Y-C, Tai C-K 2016 Promotion of
550 metastasis of thyroid cancer cells via NRP-2-mediated induction. Oncol Lett
551 **12**:4224–4230.
552 38. Antonica F, Kasprzyk DF, Opitz R, Iacovino M, Liao X-H, Dumitrescu AM, Refetoff
553 S, Peremans K, Manto M, Kyba M, Costagliola S 2012 Generation of functional
554 thyroid from embryonic stem cells. Nature **491**:66–71.
555 39. Chopra K, Ishibashi S, Amaya E 2019 Zebrafish duox mutations provide a model
556 for human congenital hypothyroidism. Biol Open **8**.
557 40. Anelli V, Villefranc JA, Chhangawala S, Martinez-McFaline R, Riva E, Nguyen A,
558 Verma A, Bareja R, Chen Z, Scognamiglio T, Elemento O, Houvras Y 2017

559 Oncogenic BRAF disrupts thyroid morphogenesis and function via twist
560 expression. Elife **6**.
561 41. Singh SP, Janjuha S, Chaudhuri S, Reinhardt S, Kränkel A, Dietz S, Eugster A,
562 Bilgin H, Korkmaz S, Zararsız G, Ninov N, Reid JE 2018 Machine learning based
563 classification of cells into chronological stages using single-cell transcriptomics.
564 Sci Rep **8**:17156.
565 42. Butler A, Hoffman P, Smibert P, Papalexi E, Satija R 2018 Integrating single-cell
566 transcriptomic data across different conditions, technologies, and species. Nat
567 Biotechnol doi: 10.1101/164889.
568 43. Varshney GK, Pei W, LaFave MC, Idol J, Xu L, Gallardo V, Carrington B, Bishop
569 K, Jones M, Li M, Harper U, Huang SC, Prakash A, Chen W, Sood R, Ledin J,
570 Burgess SM 2015 High-throughput gene targeting and phenotyping in zebrafish
571 using CRISPR/Cas9. Genome Res **25**:1030–42.
572 44. Huang D, Sherman BT, Tan Q, Collins JR, Alvord WG, Roayaei J, Stephens R,
573 Baseler MW, Lane HC, Lempicki RA 2007 The DAVID Gene Functional
574 Classification Tool: a novel biological module-centric algorithm to functionally
575 analyze large gene lists. Genome Biol **8**:R183.
576
577

Acknowledgements

We thank members of the Costagliola and Singh lab for comments on the manuscript, members of Center for Regenerative Therapies Dresden (CRTD) fish, FACS and sequencing facility, and members of IRIBHM fish facility for technical assistance. We thank J.-M. Vanderwinden from the Light Microscopy Facility and Christine Dubois from the FACS facility for technical assistance at ULB. We are grateful to Priyanka Oberoi for illustrations. P.G is Fund for Research in the Industry and the Agriculture (FRIA) Research fellow; M.S. is FNRS Research Fellow (34985615 - THYSCEFA); S.C. is FNRS Senior Research Associate. V.D. acknowledges grants from the Fond Naets (J1813300), the Fondation Contre le Cancer (2016-093) and FNRS (EQP/OL U.N019.19, J006120F). Work by M.B., C.L. and G.K. was supported by grants to M.B. from the Deutsche Forschungsgemeinschaft and European Union (European Research Council AdG Zf-BrainReg). Work by S.P.S. was supported by MISU funding from the FNRS (34772792 – SCHISM). This work was supported by grants from the Belgian National Fund for Scientific Research (FNRS) (FRSM 3-4598-12; CDR-J.0145.16, GEQ U.G030.19), the Fonds d'Encouragement à la Recherche de l'Université Libre de Bruxelles (FER-ULB).

Author contribution

S.P.S. conceptualized the project. G.K., C.L. and M.B. provided animals for single-cell RNA-Sequencing. S.P.S., S.R., A.K., J.B., and A.P. performed the single-cell RNA-Sequencing. S.P.S., S.E.E., V.D., S.C. analysed and interpreted the data. S.P.S. developed the online browser. P.G. generated the *pax2a* knock-in line. P.G. and M.S.

analysed the *pax2a* reporter line. S.P.S. wrote the first draft and P.G. edited the manuscript. S.P.S. acquired funding for the project. All authors read and approved the final manuscript.

Conflict of interest

The authors declare no competing interests.

Figure Legends

Figure 1: Single-cell RNA-Seq. of the zebrafish thyroid gland

(A – B) A brightfield image showing the zebrafish thyroid gland along with surrounding tissue. The thyroid gland surrounds the ventral aorta, which extends from the outflow tract of the heart into the gills towards the lower jaw. The thyroid follicular cells, or thyrocytes, are labeled in green in the *Tg(tg:nls-mVenus-NTR)* transgenic line (B'). **(C)** A t-SNE plot displaying the 6249 single-cells profiled in the zebrafish thyroid gland atlas. The colors represent cell clusters denoting a specific cell-type. **(D – F)** Cluster #1 represents the thyrocytes that express *tg*, *slc5a5* (NIS) and *tpo*.

Figure 2: Gene expression signature of the different cell-types in the zebrafish thyroid gland

(A) Heatmap depicting five genes specifically expressed in each one of the seven clusters of the zebrafish thyroid gland atlas. **(B – G)** t-SNE plots overlaid with the expression of a gene specific to each of the cluster. The endothelium cluster (cluster #2) is a mix of blood vessels and lymphatic vessels (see Supp. Fig. 4), while the immune cell cluster (cluster #4) is a mix of macrophages, neutrophils and lymphocytes (see Supp. Fig. 5).

Figure 3: Connectome of the zebrafish thyroid gland identifies a dense intercellular signaling network

(A) To build a connectome for the atlas, the ligands expressed specifically in each cell-type were matched with their corresponding receptors in the thyrocytes. **(B)** A highly

connected intercellular interaction network is identified by the connectome. The number of ligand-receptor pairs identified between two cell-types is denoted alongside the arrows. **(C)** A dotplot depicting examples of paracrine and autocrine signaling in the thyroid gland. The dots represent expression level in the different cell-types of the atlas.

Figure 4: Thyrocytes can be subdivided into two transcriptionally distinct sub-populations

(A) Unsupervised clustering of the thyrocyte population identifies two sub-populations. **(B)** Heatmap depicting the top ten most differentially expressed genes between the two sub-populations. **(C)** Violin plots depicting the expression levels of three specific genes in each sub-populations. Y-axis represents scaled data.

Figure 5: *pax2a*^{mKO2} knock-in line faithfully reports *pax2a* expression and knock-down

(A) Schematic of the knock-in strategy used to generate the *pax2a*^{mKO2} line. Double strand break was induced between the penultimate codon and the STOP codon of *pax2a* gene using CRISPR/Cas9. DNA repair integrates the donor construct at the site of double strand break, resulting in a *pax2a* reporter line. The donor construct contains T2A-mKO2 reporter cassette flanked by left homology (LH) and right homology (RH) arms. **(B)** Whole mount immunofluorescence of 9.5hpf *pax2a*^{mKO2} embryos stained with anti-mKO2 antibody (red) and anti-PAX2A antibody (green). Anterior is to the left, and dorsal side is to the top. **(C)** Whole mount immunofluorescence of 55 hpf *pax2a*^{mKO2}; *Tg(tg:nls-EGFP)* stained with PAX2A antibody (PAX2A-Ab) displays an overlap of mKO2 and PAX2A-Ab signal. The otic vesicle (OV), mid-hindbrain barrier (MHB), interneurons (IN) and thyroid

gland (THY) is labelled. **(D – F)** Confocal microscopy imaging of a sagittal section of a 55 hpf *pax2a*^{mKO2}; *Tg(tg:nls-EGFP)* embryos showing co-localization of mKO2 and *pax2a* in the pronephros (D), thyroid gland (E) and mid-hindbrain barrier (F). In the thyroid gland, mKO2, PAX2A-Ab and thyrocyte-specific GFP (green) show co-localization. Scale bars: 100µm (C) and 50µm (D – F). Anterior to the right, white dashed line represents the outline of the embryo. **(G – H)** Snapshots from live imaging of 55 hpf *pax2a*^{mKO2}; *Tg(tg:nls-EGFP)* embryos injected with sgRNA targeting *pax2a* coding sequence. The anterior part of a representative control embryo (G) is shown alongside a representative crispant (H). Crispants display a strong reduction of mKO2 fluorescence, as well as an absence of GFP signal suggesting absence of thyroid (THY) tissue.

Figure 6: A *pax2a* knock-in line validates the presence of thyrocyte sub-populations

(A-D) Analysis of 3 mpf thyroid gland from *pax2a*^{mKO2} zebrafish shows heterogeneity in *pax2a* reporter expression. **(A)** Whole mount confocal imaging of a 3 mpf *pax2a*^{mKO2} thyroid labelled with mKO2 (red), E-cadherin (cyan, not shown in 'A' for clarity reasons) and DAPI (dark blue) for nuclear localisation. **(B – D)** Optical sections of three follicles, with mKO2-Low cells labelled with arrows. E-cadherin (B' – D') and DAPI (B'' – D'') staining shows that absence of mKO2 signal does not correspond to an absence of cells. Scale bars: 250 µm (A), 50 µm (B – D). Anterior to the bottom of the pictures. **(E – G)** Cells from the thyroid gland of 5 mpf *Tg(tg:nls-GFP); pax2a*^{mKO2} animals were labelled with calcein (live cell marker) and analysed using FACS. (E) A FACS plot showing calcein on X-axis and GFP on Y-axis. The box encompassing the GFP+ cells represents the thyrocyte population, which was gated for further analysis. (F) Histogram showing the

671 distribution of GFP intensity in thyrocytes. (G) Histogram showing the distribution of
672 mKO2 intensity in thyrocytes. Thyrocytes were selected by gating for GFP+ population.
673 Horizontal lines indicate the mKO2-Low and mKO2-High expression level, with
674 percentage values representing proportion of thyrocytes with mKO2-Low and mKO2-High
675 expression.

Figure 1

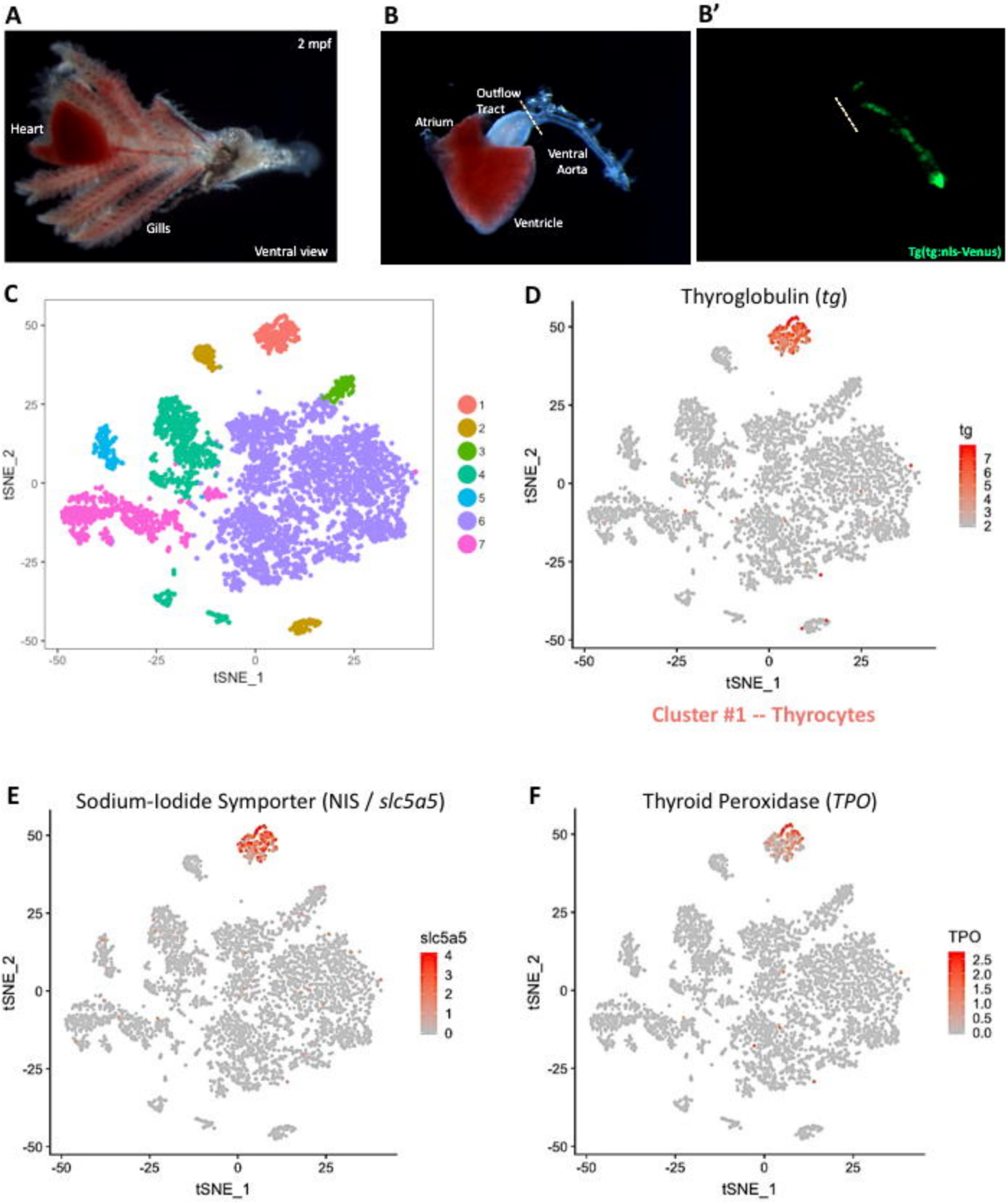

Figure 2

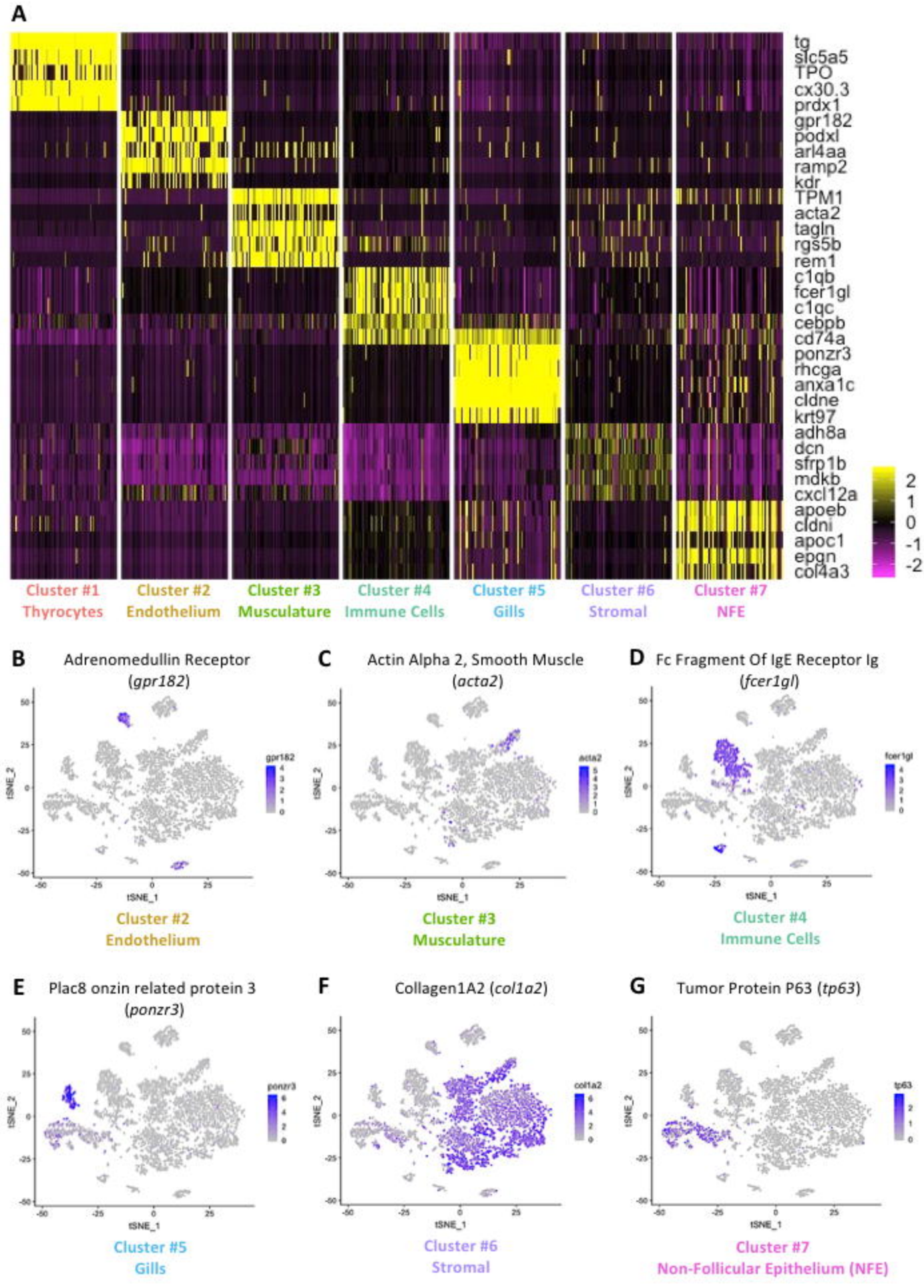

Figure 3

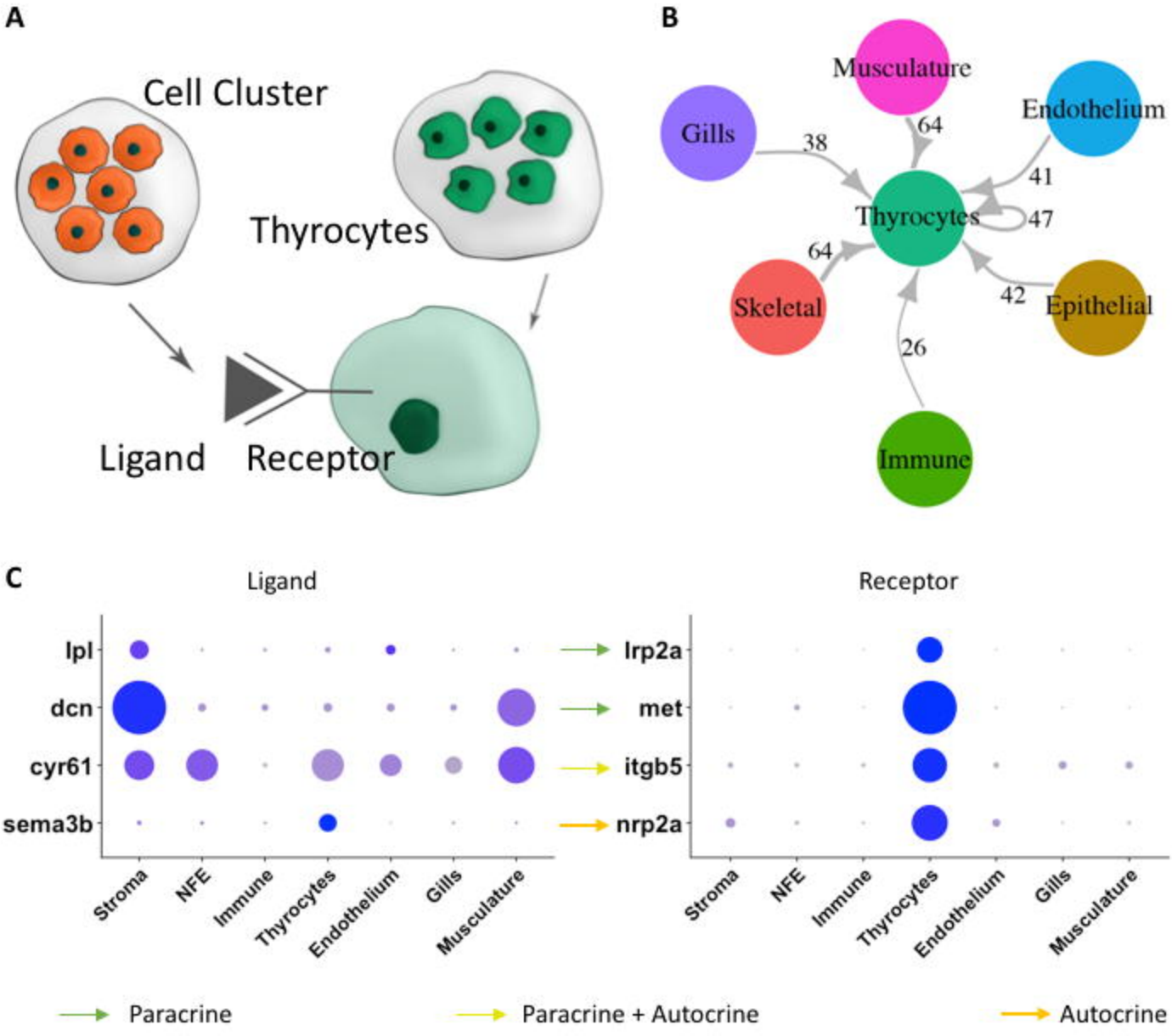

Figure 4

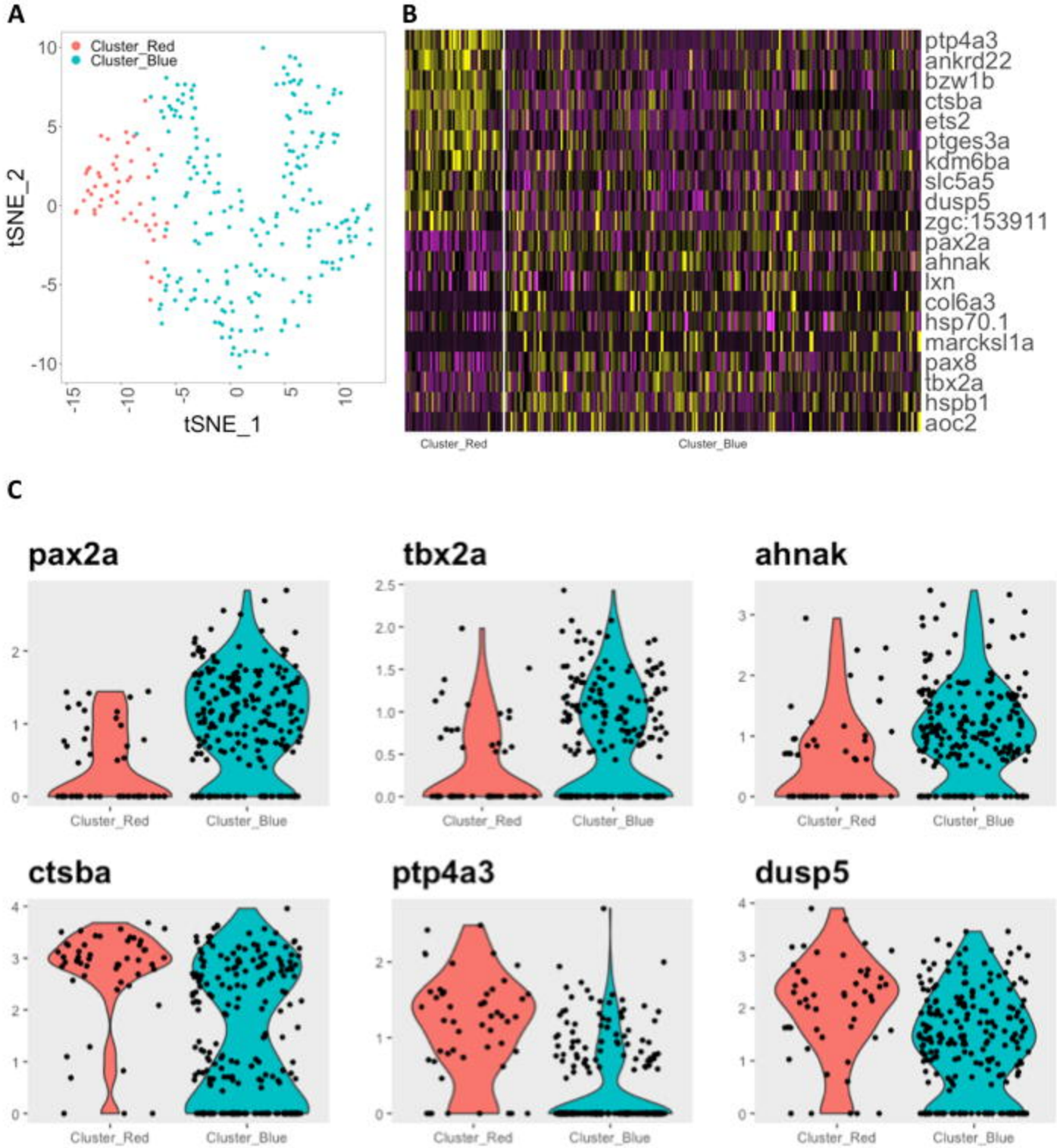

Figure 5

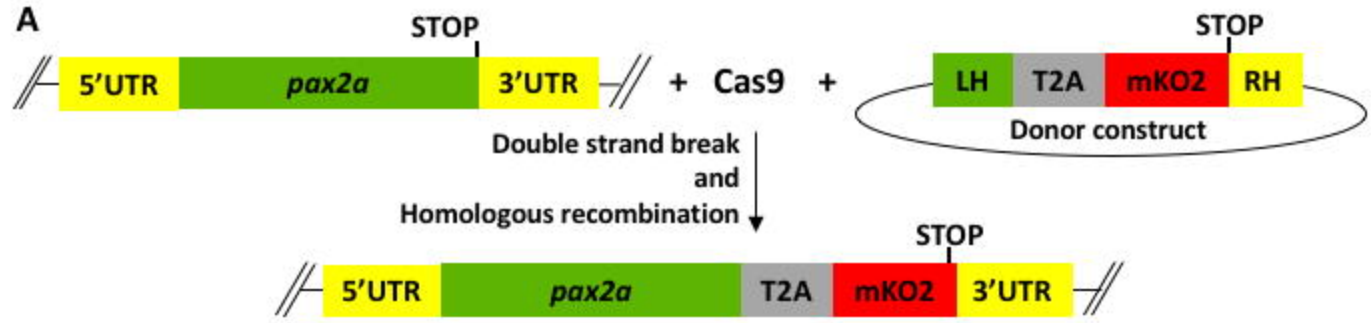

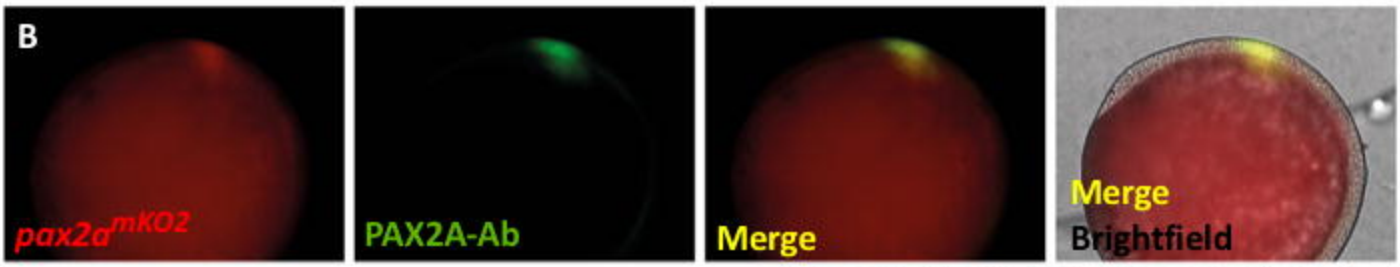

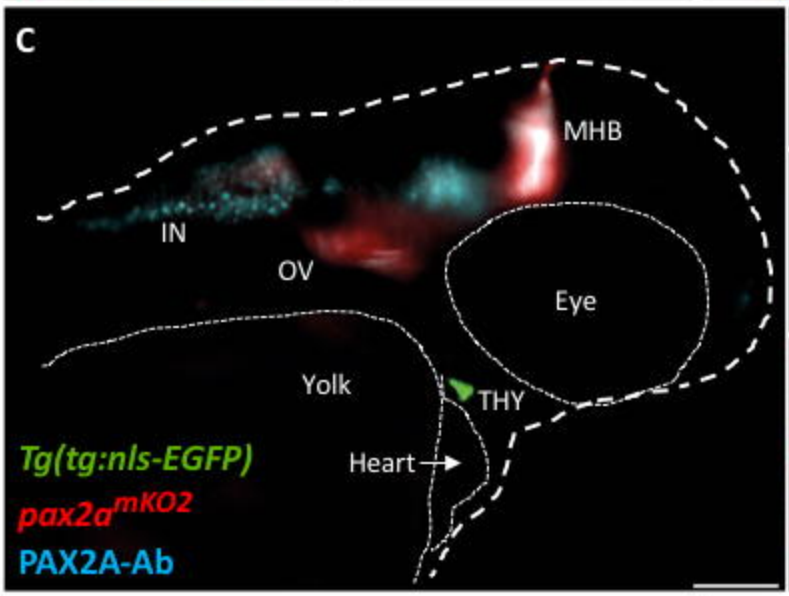

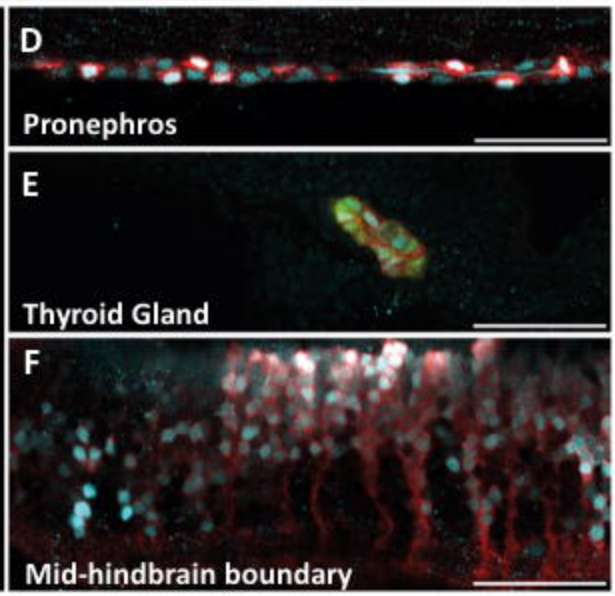

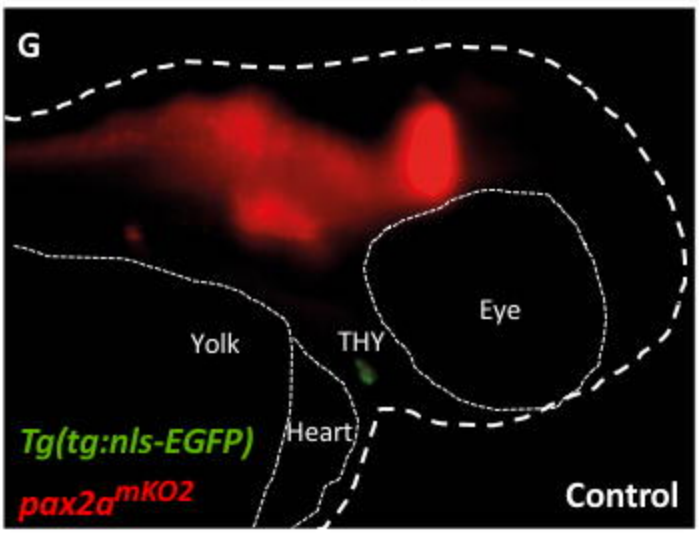

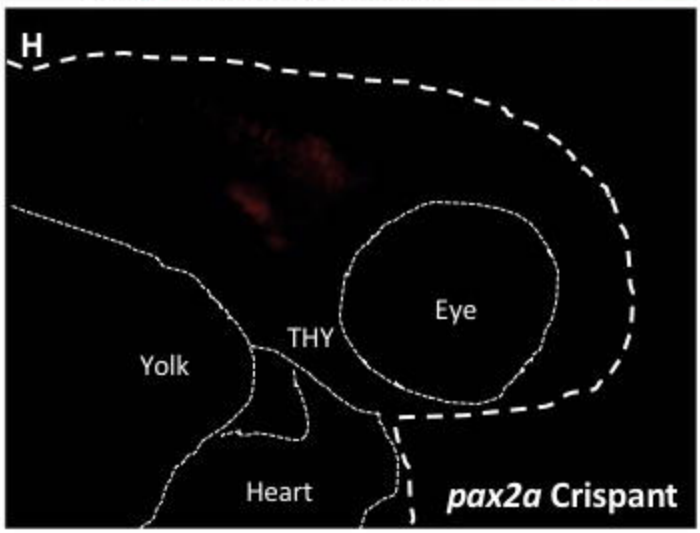

Figure 6